Highlights

A Physics Informed Machine Learning Framework for Optimal Sensor Placement and Parameter Estimation

Georgios Venianakis, Constantinos Theodoropoulos, Michail Kavousanakis

- A PINN framework for joint sensor placement and parameter estimation is presented.

- Sensor locations are optimized using sensitivity functions and D-optimal design.

- The framework is demonstrated for reaction-diffusion-advection systems.

- Optimal placement yields improved parameter estimates over heuristic choices.

A Physics Informed Machine Learning Framework for Optimal Sensor Placement and Parameter Estimation

Georgios Venianakis*a*, Constantinos Theodoropoulos*a,b,∗* and Michail Kavousanakis*a,∗*

aSchool of Chemical Engineering, National Technical University of Athens, Iroon Polytechneiou 9, Athens, 15772, Greece

bDepartment of Chemical Engineering, University of Manchester, Manchester, M13 9PL, United Kingdom

ARTICLE INFO

Keywords:
Machine Learning
Physics Informed Neural Networks
D-optimality
distributed-parameter systems
Fisher Information matrix
automatic differentiation

ABSTRACT

Parameter estimation remains a challenging task across many areas of engineering. Because data acquisition can often be costly, limited, or prone to inaccuracies (noise, uncertainty) it is crucial to identify sensor configurations that provide the maximum amount of information about the unknown parameters, in particular for the case of distributed-parameter systems, where spatial variations are important. Physics-Informed Neural Networks (PINNs) have recently emerged as a powerful machine-learning (ML) tool for parameter estimation, particularly in cases with sparse or noisy measurements, overcoming some of the limitations of traditional optimization-based and Bayesian approaches. Despite the widespread use of PINNs for solving inverse problems, relatively little attention has been given to how their performance depends on sensor placement. This study addresses this gap by introducing a comprehensive PINN-based framework that simultaneously tackles optimal sensor placement and parameter estimation. Our approach involves training a PINN model in which the parameters of interest are included as additional inputs. This enables the efficient computation of sensitivity functions through automatic differentiation, which are then used to determine optimal sensor locations exploiting the D-optimality criterion. The framework is validated on two illustrative distributed-parameter reaction-diffusion-advection problems of increasing complexity. The results demonstrate that our PINNs-based methodology consistently achieves higher accuracy compared to parameter values estimated from intuitively or randomly selected sensor positions.

⋆

∗Corresponding authors

✉ k.theodoropoulos@manchester.ac.uk (C. Theodoropoulos); mihkavus@chemeng.ntua.gr (M. Kavousanakis)

ORCID(s):

Nomenclature

NN	Neural Network
PINN	Physics Informed Neural Network
FIM	Fisher Information Matrix
AD	Automatic Differentiation
RAR-D	Residual-based Adaptive Refinement with Distribution
FEM	Finite Element Method
$\mathbf{u}$	General state variable(s)
λ	Unknown parameters vector
λ^{prior}	A priori parameter estimate vector
s_{λ_j}	Sensitivity function to the parameter λ_j
F	FIM
$\mathbf{x}_1^*, \dots, \mathbf{x}_N^*$	Selected spatial coordinates of N sensors
$\tilde{\ }$	Dimensionless form of a variable
$\hat{\mathbf{u}}$	Approximation of $\tilde{\mathbf{u}}$ (Numerical or PINN)
θ	NN's trainable parameters (weights and biases)
$\mathcal{L}(\theta)$	NN's total loss function
$\mathcal{L}_f(\theta)$	Loss function term corresponding to the PDE residual(s)
$\mathcal{L}_{ic}(\theta)$	Loss function term corresponding to the initial condition residual
$\mathcal{L}_{bc}(\theta)$	Loss function term corresponding to the boundary conditions residuals
$\mathcal{L}_{sens}(\theta)$	Loss function term corresponding to the sum of partial derivatives of all residuals w.r.t. all the parameters of interest
c	Species concentration (kg/m^3)
$\mathbf{v}$	Velocity Field (m/s)
p	Pressure (Pa)
D	Diffusion coefficient (m^2/s)
k	Reaction rate constant of an n-th order reaction ($(kg/m^3)^{1-n} \cdot s^{-1}$)
U	Fluid's mean inlet velocity (m/s)
ρ	Fluid density (kg/m^3)
μ	Fluid viscosity ($Pa \cdot s$)
τ	Characteristic time scale (s)
Pe	Péclet number
Da	Damköhler number
Re	Reynolds number

1. Introduction

Distributed-parameter systems, based on partial differential equations (PDEs), typically describing spatiotemporal variations, represent a wide range of physical systems and phenomena in science and engineering. These PDE-based models typically involve multiple unknown parameters, often corresponding to physical properties of the system, whose accurate identification from available data is essential for reliable prediction and effective system design. In general, the accuracy of parameter estimation improves as more data is collected. Nevertheless, acquiring large datasets is often expensive or impractical. This motivates the development of systematic methods for selecting sensor locations that maximize the information gained about the unknown parameters under constraints on the number of sensors.

Most research on Optimal Sensor Placement has focused on state estimation, while comparatively fewer studies have addressed parameter estimation directly (Alaña and Theodoropoulos, 2011, 2012). Existing approaches typically rely on scalar measures derived from the Fisher Information Matrix (FIM), which captures the sensitivity of observable quantities with respect to parameters. For example, the modified E-criterion (Mehra, 1974; Walter and Pronzato, 1990; Nahor et al., 2003) minimizes the ratio of the largest to the smallest eigenvalue of the FIM, while Heredia-Zavoni and Esteva (1998) proposed minimizing the expected Bayesian loss involving the trace of the inverse FIM. The widely used D-optimality criterion (Qureshi et al., 1980; Vande Wouwer et al., 2000) maximizes the determinant of the FIM (or

the Gram determinant), and a closely related approach minimizes the information entropy (Papadimitriou et al., 2000), reflecting the uncertainty of the parameter under a given sensor configuration.

In large-scale distributed systems, parameter estimation can be facilitated by combining model reduction with optimal sensor placement. In Alonso et al. (2004), the proposed workflow is to construct a Proper Orthogonal Decomposition (POD) reduced-order model that captures the dominant spatio-temporal dynamics and then determine measurement locations by optimizing an observability-based criterion on this reduced model. Alaña and Theodoropoulos (2011) further streamline this process by proposing sensor placement directly at the extrema of the dominant POD modes, an approach that circumvents costly sensitivity-matrix computations while still providing near-optimal parameter estimation performance.

Once sensor locations are defined, the next step is parameter estimation. Optimization-based methods, such as Maximum Likelihood Estimation (MLE) (Myung, 2003), remain the most established, with Least Squares as the most common implementation under the assumption of Gaussian measurement noise (Biegler et al., 1986; Englezos and Kalogerakis, 2000). While effective, these methods typically require repeated model evaluations, resulting in high computational cost, particularly when gradients with respect to parameters must also be computed. Moreover, the accuracy of estimated parameters may degrade under sparse or noisy data (Kravaris et al., 2013). Bayesian methods offer an alternative by incorporating prior information and providing full uncertainty quantification through posterior distributions (Coleman and Block, 2006; Hermanto et al., 2008; Kalyanaraman et al., 2015). Nevertheless, Bayesian inference often relies on Markov Chain Monte Carlo (MCMC) sampling (Hastings, 1970), which requires extensive forward model evaluations and can be sensitive to prior selection in data-limited settings (Lenk and Orme, 2009).

Recent advances in machine learning have substantially enhanced the field of parameter estimation by introducing data-driven methodologies capable of capturing complex relationships between model parameters and observed data. Traditional statistical approaches, such as maximum likelihood estimation and Bayesian inference, have been extended through modern techniques, such as variational inference (Blei et al., 2017) and neural density estimation (Papamakarios et al., 2021) that enable efficient and accurate parameter recovery, even in complex or high-dimensional settings. Furthermore, deep neural architectures, coupled with gradient-based optimization algorithms, including stochastic gradient descent and its adaptive variants (Bottou, 2010), facilitate scalable and robust inference across a wide range of applications.

Hybrid modeling frameworks that integrate data with first-principles formulations have merged as powerful tools for scientific computing. Among these, Physics-Informed Neural Networks (PINNs) (Raissi et al., 2019) exploit the expressivity of deep neural networks (Hornik et al., 1989) while embedding governing PDEs as soft constraints. PINNs have proven particularly useful in scenarios where traditional solvers face challenges: complex geometries (since PINNs are mesh-free), high-dimensional problems (Hu et al., 2024). and systems with incomplete physics that require data-driven enhancement (Raissi et al., 2020). Importantly, PINNs enable parameter estimation by directly incorporating unknown parameters into the training process, making them robust even under sparse or noisy observations, which is of particular relevance to this work.

Numerous studies have applied PINNs to inverse problems in chemical engineering and related fields. Examples include the estimation of thermal properties in additive manufacturing (Liao et al., 2023), thermal diffusivity in two-phase flows (Cai et al., 2021), kinetic parameters in catalytic reactors (Ngo and Lim, 2021; Huang et al., 2025), and transport coefficients in porous media (Berardi et al., 2025). PINNs have also been used in fluid mechanics, such as inferring density fields in high-speed flows (Mao et al., 2020) and thrombus properties in arterial flows (Yin et al., 2021).

Despite these successes, most studies assume dense observations across the spatial domain, often generated from numerical simulations, overlooking the constraints of real-world sensor settings. For instance, Ngo and Lim (2021) observed that parameter estimation accuracy strongly depends on the spatial region from which data is collected, but this conclusion was based on manual experimentation rather than systematic sensor placement strategies. The integration of optimal sensor placement with PINNs remains relatively unexplored. A few attempts have been made: Forootani et al. (2024) proposed a greedy sampling approach (GS-PINN), which selects informative samples via Proper Orthogonal Decomposition (POD) and the Discrete Empirical Interpolation (DEIM) method (Chaturantabut and Sorensen, 2010), but their approach requires access to full spatio-temporal data and selects time-varying sensor positions, limiting practical use. In Chang et al. (2025), they introduce a sensitivity-based sampling method (SBS) that adapts sensor placement based on gradients of the PINN loss with respect to collocation points. However, this method was designed for state reconstruction problems in process control, not parameter estimation, as it does not account for sensitivities with respect to the parameters.

In this work, we address this gap by proposing a PINN framework that integrates D-optimal sensor placement directly into the parameter estimation process. Our approach relies on two complementary neural network models. The first model incorporates the parameters of interest as inputs, enabling the computation of sensitivity functions via automatic differentiation (AD). These sensitivities are used to select optimal sensor locations under the D-optimality criterion. The second, is a standard PINN model trained on data obtained from these optimal locations to perform parameter estimation and state reconstruction.

We demonstrate our method on two illustrative case studies involving reaction-diffusion-advection systems of increased complexity: a one-dimensional steady-state problem, and a two-dimensional transient problem. In each case, the goal is to estimate important dimensionless parameters for the system such as the Péclet number and Damköhler number and to compare their accuracy against estimations made from sub-optimal sensor locations.

The paper is organised as follows: Section 2 presents the formulation of our method, including sensor selection and PINN training. Section 3 describes the case studies and results. Finally, Section 4 discusses the main conclusions and the relevant future directions.

2. Methods
2.1. Selection of Optimal Sensor Location for Parameter Estimation

In this work, we adopt the D-optimality criterion, widely used for sensor placement due to its geometric interpretability and invariance to parameter rescaling (Franceschini and Macchietto, 2008; Bard, 1974). For implementation, we follow the method of Vande Wouwer et al. (2000), chosen for its simplicity. Alternative optimality criteria can also be applied as discussed in (Alaña and Theodoropoulos, 2011).

Consider a system with states $\mathbf{u}(\mathbf{x}, t)$ described by the governing PDE:

$$\frac{\partial \mathbf{u}}{\partial t} + \mathcal{N}[\mathbf{u}; \lambda] = 0, \quad \mathbf{x} \in \Omega, \quad t \geq 0, \tag{1}$$

subject to the following initial and boundary conditions:

$$\mathbf{u}(0, \mathbf{x}) = \mathbf{g}(\mathbf{x}), \quad \mathbf{x} \in \Omega, \tag{2}$$

$$\mathcal{B}[\mathbf{u}] = 0, \quad \mathbf{x} \in \partial\Omega, \quad t \geq 0, \tag{3}$$

where $\mathcal{N}[\cdot]$ is a differential operator, and $\mathcal{B}[\cdot]$ a boundary operator, $\lambda = [\lambda_1, \ldots, \lambda_P]$ are the p unknown parameters, and Ω the spatial domain.

For state measurements at N sensor locations $\mathbf{x}_1, \ldots, \mathbf{x}_N$ we define sensitivity functions as:

$$s_{\lambda_j}(\mathbf{x}_i, t) = \frac{\partial \mathbf{u}}{\partial \lambda_j}(\mathbf{x}_i, t), \ i = 1, \ldots, N, \ j = 1, \ldots, P, \tag{4}$$

and collect them into a vector M:

$$M(x_1, \ldots, x_N, t) = \left[s_{\lambda_1}(\mathbf{x}_1, t) \ \ldots \ s_{\lambda_P}(\mathbf{x}_1, t) \ \ldots s_{\lambda_1}(\mathbf{x}_N, t) \ \ldots \ s_{\lambda_P}(\mathbf{x}_N, t) \right]^T. \tag{5}$$

The Fisher Information Matrix, F, is then:

$$F(\mathbf{x}_1, \ldots, \mathbf{x}_N) = \int_0^T M(x_1, \ldots, x_N, t) M^T(x_1, \ldots, x_N, t) \, dt, \tag{6}$$

where $[0, T]$ is the observation horizon. The matrix F is positive semi-definite with its diagonal entries quantifying sensor sensitivity to parameters, while its off-diagonal entries capture correlations between the corresponding parameters.

The optimal sensor locations $\mathbf{x}_1^*, \ldots, \mathbf{x}_N^*$ maximize the Gram determinant (Courant and Hilbert, 1989):

$$\mathbf{x}_1^*, \ldots, \mathbf{x}_N^* = \arg \max_{\mathbf{x}_1, \ldots, \mathbf{x}_N} \det \left[F(\mathbf{x}_1, \ldots, \mathbf{x}_N) \right]. \tag{7}$$

Maximizing $\det(F)$ encourages both large sensitivities (via diagonal dominance) and independence (via small off-diagonal terms).

For *steady-state* problems the FIM reduces to:

$$F(\mathbf{x}_1, \ldots, \mathbf{x}_N) = M(x_1, \ldots, x_N, t) M^T(x_1, \ldots, x_N, t), \tag{8}$$

which is rank-1 with zero determinant, rendering D-optimality unusable. For these cases, we instead select optimal sensor locations by maximizing the FIM trace:

$$\mathbf{x}_1^*, \ldots, \mathbf{x}_N^* = \arg \max_{\mathbf{x}_1, \ldots, \mathbf{x}_N} \operatorname{tr} \left[F(\mathbf{x}_1, \ldots, \mathbf{x}_N) \right]. \tag{9}$$

Our PINN framework as well as the calculation of sensitivities using PINNs is discussed next.

2.2. Physics Informed Neural Networks: General Framework

PINNs are fully connected neural networks that incorporate PDE constraints into their loss function (Wang et al. (2023)). They address two problem types:

(a) **Forward Problems:** approximating PDE solutions with known parameters and boundary/initial conditions, without experimental data.
(b) **Inverse Problems:** estimating unknown parameters from experimental data, while simultaneously approximating the PDE solution.

For the forward problem, the system state $\mathbf{u}(t, \mathbf{x})$ governed by Eqs. (1)–(3) is approximated by a neural network $\hat{\mathbf{u}}(t, \mathbf{x}, \theta)$, where θ denotes trainable weights and biases. Training minimizes a composite loss function, $\mathcal{L}$:

$$\mathcal{L}(\theta) = \mathcal{L}_f(\theta) + \mathcal{L}_{ic}(\theta) + \mathcal{L}_{bc}(\theta), \tag{10}$$

with terms enforcing PDE residuals ($\mathcal{L}_f$), initial conditions ($\mathcal{L}_{ic}$), and boundary conditions ($\mathcal{L}_{bc}$). Automatic differentiation computes derivatives of the system state required for residual evaluation (PDE and boundary conditions residuals).

For *inverse problems*, observational data $\left\{ \mathbf{u}_{data}^i \right\}_{i=1}^{N_{data}}$ at spatio-temporal coordinates $\left\{ t_{data}^i, \mathbf{x}_{data}^i \right\}_{i=1}^{N_{data}}$ introduce an additional loss term:

$$\mathcal{L}_{data}(\theta) = \frac{1}{N_{data}} \sum_{i=1}^{N_{data}} \left| \hat{\mathbf{u}}(t_{data}^i, \mathbf{x}_{data}^i) - \mathbf{u}_{data}^i \right|^2, \tag{11}$$

leading to the total loss function:

$$\mathcal{L}(\theta) = \mathcal{L}_{ic}(\theta) + \mathcal{L}_{bc}(\theta) + \mathcal{L}_f(\theta) + \mathcal{L}_{data}(\theta). \tag{12}$$

In this case, PINNs are optimized with respect to both θ and unknown parameters λ.
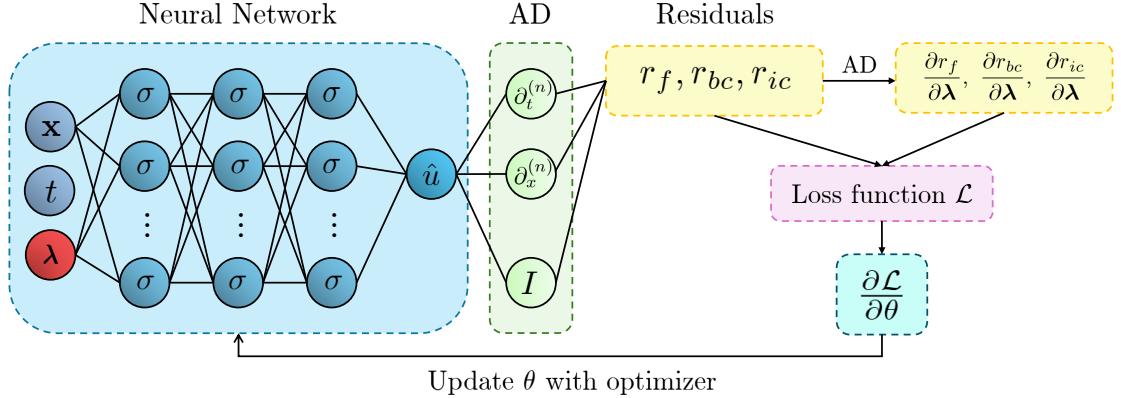
Figure 1: Schematic representation of the methodology for computing sensitivity derivatives using PINNs. The neural network admits as input the spatio-temporal coordinates $(\mathbf{x}, t)$ along with the parameters of interest, λ. The loss function $\mathcal{L}$ to be minimized is constructed from the system residuals (PDE and boundary/initial conditions) and their derivatives with respect to the parameters, λ.

2.3. Sensitivity functions with PINNs

As described in Section 2.1, optimal sensor placement requires sensitivity functions (Eq. (4)). Following Hanna et al. (2024), the PINN input is extended to include both spatio-temporal coordinates and parameters λ, enabling AD-based computation of $\partial \hat{\mathbf{u}} / \partial \lambda_j$. Additional loss terms enforce accurate parameter sensitivities calculation:

$$\mathcal{L}(\theta) = \mathcal{L}_{ic}(\theta) + \mathcal{L}_{bc}(\theta) + \mathcal{L}_f(\theta) + \mathcal{L}_{sens,ic}(\theta) + \mathcal{L}_{sens,bc}(\theta) + \mathcal{L}_{sens,f}(\theta), \tag{13}$$

where:

$$\mathcal{L}_{sens,ic}(\theta) = \frac{1}{N_{ic}} \sum_{j=1}^{P} \sum_{i=1}^{N_{ic}} \left| \frac{\partial r_{ic}}{\partial \lambda_j}(0, \mathbf{x}_{ic}^i, \lambda, \theta) \right|^2, \tag{14}$$

$$\mathcal{L}_{sens,bc}(\theta) = \frac{1}{N_{bc}} \sum_{j=1}^{P} \sum_{i=1}^{N_{bc}} \left| \frac{\partial r_{bc}}{\partial \lambda_j}(t_{bc}^i, \mathbf{x}_{bc}^i, \lambda, \theta) \right|^2, \tag{15}$$

$$\mathcal{L}_{sens,f}(\theta) = \frac{1}{N_f} \sum_{j=1}^{P} \sum_{i=1}^{N_f} \left| \frac{\partial r_f}{\partial \lambda_j}(t_f^i, \mathbf{x}_f^i, \lambda, \theta) \right|^2. \tag{16}$$

Each $\mathcal{L}_{sens,\cdot}$ term penalizes derivatives of residuals with respect to λ.

Training is performed with prior parameter estimates, λ^{prior}. The resulting sensitivity functions are then used to construct the FIM and determine optimal sensor locations. Here we assume that their qualitative structure (e.g., locations of maxima) remains the same when evaluated at λ^{prior} compared to the true λ. When the computed optima differ substantially, we use an iterative approach. Fig. 1 illustrates the process.

Once sensor placement is decided, state data are collected from the corresponding locations, and the inverse problem is solved using PINNs. To accelerate training, we apply transfer learning (Zhuang et al., 2021): the inverse PINN is initialized from a pretrained forward PINN at prior parameter values, λ^{prior}. A lightweight fine-tuning strategy is adopted here (Goswami et al., 2020), which retrains only the last hidden layers while freezing the earlier ones, reducing both the number of epochs and the per-iteration cost.

Finally, to improve PINN training efficiency and stability we incorporate techniques including:

- **Dynamic loss weighting:** Following Li and Feng (2022), loss weights w_k multiplying each loss term in the loss function are adaptively updated to balance gradients across different terms, preventing dominance by any single component (see e.g., Eq. (18) and Eq. (31) below).

- **Residual-based adaptive refinement (RAR-D):** Collocation points are adaptively chosen according to the PDE residual (Wu et al., 2023), focusing training on regions with higher errors. We extend this strategy to boundary and initial condition sampling (collocation) points as well.

- **Non-dimensionalization:** PDEs are solved in dimensionless form, preventing vanishing/exploding gradients and ensuring balanced loss contributions across variables (Wang et al., 2023).

3. Case Studies

This section presents two illustrative examples that demonstate our PINNs-based methodology and also showcase how the optimal sensor placement criterion enhances parameter inference accuracy. All PINN models are implemented in Python using the PyTorch® library (Paszke et al., 2019) and trained on an NVIDIA® RTX A4000 GPU computer.

3.1. 1D Steady State Reaction–Advection–Diffusion equation
3.1.1. *Problem Set-Up*
The first simpler example considers a steady state, one-dimensional reaction-advection-diffusion equation, which in dimensionless form is given by the following PDE and boundary conditions:

$$Pe\frac{dc}{dx} = \frac{d^2c}{dx^2} - Dac^2, \ x \in [0, 10],$$
$$c(0) = 1, \quad (17)$$
$$\frac{dc}{dx}\bigg|_{x=L} = 0,$$

where Pe and Da denote the Péclet number and the Damköhler number, respectively. In this example, Da is fixed ($Da = 1.0$), and the goal is to estimate the unknown value of Pe with a single, optimally placed sensor.

3.1.2. *PINN Framework*
To compute sensitivities for the FIM construction, we employ a Sensitivity PINN model with two inputs (x and Pe), four hidden layers of 30 neurons each, and hyperbolic tangent activation. This network structure is chosen to balance computational efficiency with accuracy. The loss function is

$$\mathcal{L}(\theta) = w_f \mathcal{L}_f(\theta) + w_{bc1}\mathcal{L}_{bc1}(\theta) + w_{bc2}\mathcal{L}_{bc2}(\theta) + w_{sens}\left(\mathcal{L}_{sens,f}(\theta) + \mathcal{L}_{sens,bc1}(\theta) + \mathcal{L}_{sens,bc2}(\theta)\right), \quad (18)$$

where $\mathcal{L}_f(\theta)$, $\mathcal{L}_{bc1}(\theta)$, $\mathcal{L}_{bc2}(\theta)$ correspond to the PDE and boundary condition residuals. The terms $\mathcal{L}_{sens,f}(\theta)$, $\mathcal{L}_{sens,bc1}(\theta)$ and $\mathcal{L}_{sens,bc2}(\theta)$ represent the corresponding derivatives with respect to Pe. Analytical expressions are provided in Section I of the Supplementary Material. We sample 800 collocation points on an equispaced grid over the spatial domain providing sufficient resolution for our PINN model. The loss weights are dynamically updated following the gradient ascent scheme of Li and Feng (2022). Training is performed with the Adam optimizer (10^{-3} learning rate) for 2500 epochs. Since the true value of Pe is to be estimated (unknown), the model is initialized with an a priori estimate, $Pe = 0.1$. As noted in Section 2.3, we assume that the maxima of the Gram determinant (or the FIM trace in this example) are approximately invariant to whether they are computed at the estimated or true parameter values. This is equivalent to having a "reasonable" prior estimate. An iterative procedure can be employed if the computed optima vary significantly. For a single-sensor placement problem, the FIM trace reduces to the squared sensitivity of c with respect to Pe.

$$tr\left[F(x)\right] = \left[\frac{\partial c}{\partial Pe}(x)\right]^2, \ x \in [0, 10]. \quad (19)$$

Fig. 2 shows the FIM trace obtained from the PINN alongside the one obtained by numerically soving the PDE (equation 17) The results confirm that PINNs accurately compute sensitivity derivatives via automatic differentiation. Here, it is easy to locate graphically the trace maximum at $x^* = 1.81$.

Table 1
Hyperparameters of Sensitivity PINNS and Inference PINNs.

PINN Hyperparameter	Sensitivity PINN	Inference PINN
Hidden layers	4	4
Neurons per layer	30	30
Inputs	2 (x, Pe)	1 (x)
Activation function	tanh()	tanh()
Optimizer	Adam	Adam
Iterations	2500	5000
Collocation points	800	800
Dynamic weight strategy	Yes	Yes
RAR-D	No	No

Table 2
Estimated Pe values and relative error for optimal versus suboptimal sensor placement.

Sensor	Estimated Pe (true: 1.000)	Relative Error (%)
Optimal $(x^* = 1.81)$	0.998	0.20
Outlet $(x^* = 10.0)$	0.153	84.7

Consequently, pseudo-experimental data are generated numerically using the true value of $Pe = 1.0$ at two locations: the optimal location $x^* = 1.81$, and a suboptimal point at the outlet, $x^* = 10.0$, which is an intuitive choice for placing the sensor. The inference PINN has the same architecture but accepts only x as input, with Pe treated as a trainable parameter. The loss function now reads:

$$\mathcal{L}(\theta) = w_f \mathcal{L}_f(\theta) + w_{bc1} \mathcal{L}_{bc1}(\theta) + w_{bc2} \mathcal{L}_{bc2}(\theta) + w_{data} \mathcal{L}_{data}(\theta), \tag{20}$$

with the data term being:

$$\mathcal{L}_{data}(\theta) = \frac{1}{N_{data}} \sum_{i=1}^{N_{data}} \left| \hat{c}(x_{data}^i) - c_{data}^i \right|^2. \tag{21}$$

Since a single sensor is used, $N_{data} = 1$. The model is trained with the Adam optimizer for 5000 iterations. The hyperparameters for the Sensitivity and Inference PINNs applied to the 1D steady-state reaction-advection-diffusion equation are summarized in Table 1.

Fig. 3 shows the inferred Pe during training for data from the optimal and outlet locations. The results highlight the crucial role of sensor placement: the PINN converges closer to the true Pe, when data are taken at the optimal location. At the outlet, the parameter fails to converge for the number of epochs used. Final estimates and relative errors are listed in Table 2.

After identifying the parameter, we recompute the optimal sensor location using the true Pe. As shown in Fig. 4, the maximum shifts slightly to $x^* = 2.32$, very close to the original $x^* = 1.81$ supporting the assumption that sensitivity maxima remain nearly invariant when evaluated with initial parameter estimates.

3.2. 2D Transient Reaction–Advection–Diffusion, Flow Around a Fixed Obstacle
The 1D example demonstrates how our PINN-based methodology guides sensor placement and enables accurate estimation of a single parameter. To further test the robustness of the framework, we now consider a more complex 2D system that combines nonlinear reaction, advection and diffusion in the presence of an obstacle. This example introduces additional challenges: heterogeneity due to flow recirculation, transient behavior, as well as the simultaneous inference of two parameters.

In particular, we address the simultaneous estimation of the dimensionless parameters Pe and Da in a two-dimensional, time-dependent reaction-advection-diffusion system. A reactive species is transported by a steady flow past a fixed cylindrical obstacle.

3.2.1. Problem Set-Up

We consider a 2D rectangular channel of dimensions $L \times H$ ($L = 0.24$ m and $H = 0.14$ m), with flow from left to right bounded by impermeable walls at the top and bottom. A fixed cylindrical obstacle of radius $R = 0.01$ m is placed inside the channel perpendicular to the flow direction, at $\{x_0, y_0\} = \{0.09, 0.07\}$ m. The fluid is incompressible, Newtonian, and the flow is considered to be at steady-state. Its velocity, $\mathbf{v}$, and pressure, p, fields satisfy the Navier-Stokes equations (neglecting gravity):

$$\rho \left(\frac{\partial \mathbf{v}}{\partial t} + \mathbf{v} \cdot \nabla \mathbf{v} \right) = -\nabla p + \mu \nabla^2 \mathbf{v}, \tag{22}$$

subject to the incompressibility constraint:

$$\nabla \cdot \mathbf{v} = 0. \tag{23}$$

where ρ, μ denote the density and dynamic viscosity, respectively.

At the inlet, a parabolic velocity profile is imposed for the horizontal component of velocity, v_x:

$$v_x(0, y) = 6U \left[\left(\frac{y}{H} \right) - \left(\frac{y}{H} \right)^2 \right]. \tag{24}$$

with no-slip conditions at the walls (including the obstacle surface) and zero pressure at the outlet. The fluid properties are set to $\rho = 1000 \left[kg/m^3 \right]$, $\mu = 0.001 \left[Pa \cdot s \right]$ and average inlet velocity $U = 0.00125 \left[m/s \right]$.

Given the steady flow $\mathbf{v}$, the concentration $c(x, y, t)$ of a reactive species evolves according to:

$$\frac{\partial c}{\partial t} + \mathbf{v} \cdot \nabla c = D \nabla^2 c - kc^2, \ (x, y) \in [0, L] \times [0, H], \ t > 0, \tag{25}$$

where D is the diffusion coefficient and k the reaction rate constant. The initial condition is:

$$c(x, y, 0) = 0, \ (x, y) \in (0, L] \times [0, H]. \tag{26}$$

The inlet concentration profile is set to change linearly with y:

$$c(0, y, t) = \frac{y}{H} + 0.3 \left[\frac{kg}{m^3} \right], \ y \in [0, H], \ t > 0. \tag{27}$$

Zero-flux boundary conditions are applied at the impenetrable walls and the (long) outlet. A schematic of the setup is shown in Fig. 5.

By selecting as characteristic scales, L, U, and $c_0 = 1$ kg/m^3, we derive the following dimensionless variables:

$$\tilde{x} = \frac{x}{L}, \ \tilde{y} = \frac{y}{L}, \ \tilde{\mathbf{v}} = \frac{\mathbf{v}}{U}, \ \tilde{p} = \frac{p}{\rho U^2} \text{ and } \tilde{c} = \frac{c}{c_0}.$$

Typically, time is scaled using

$$\tilde{t} = \frac{tD}{L^2}.$$

However, in this problem, the diffusion coefficient D is unknown and will be determined implicitly through the dimensionless parameters. Therefore, it cannot serve as the basis for non-dimensionalizing time. Instead, we define

a characteristic time scale, τ, chosen to be of the same order of magnitude as L^2/D_0, where D_0 is an initial estimate of the diffusion coefficient. Numerical tests show that setting $\tau = 4000$ s yields good results. The dimensionless time variable is therefore defined as:

$$\tilde{t} = \frac{t}{\tau}.$$

Thus, in dimensionless form, the governing equations are:

$$\tilde{\mathbf{v}} \cdot \nabla_{\tilde{\mathbf{x}}} \tilde{\mathbf{v}} = -\nabla_{\tilde{\mathbf{x}}} \tilde{p} + \frac{1}{Re} \nabla_{\tilde{\mathbf{x}}}^2 \tilde{\mathbf{v}}, \tag{28}$$

$$\nabla_{\tilde{\mathbf{x}}} \cdot \tilde{\mathbf{v}} = 0, \tag{29}$$

$$Pe \frac{L}{\tau U} \frac{\partial \tilde{c}}{\partial \tilde{t}} + Pe \tilde{\mathbf{v}} \cdot \nabla_{\tilde{\mathbf{x}}} \tilde{c} = \nabla_{\tilde{\mathbf{x}}}^2 \tilde{c} - Da \, \tilde{c}^2, \quad \tilde{\mathbf{x}} \in [0, 1] \times [0, \frac{H}{L}], \quad \tilde{t} \geq 0, \tag{30}$$

where $Re = \frac{\rho U L}{\mu}$, $Pe = \frac{UL}{D}$ and $Da = \frac{kc_0 L^2}{D}$ are the Reynolds, Péclet and Damköhler numbers, respectively. From this point forward, tildes are omitted for convenience.

3.2.2. PINN Set-Up

Following the approach of Laubscher (2021), we construct and train separate PINN models: one for the fluid flow PDEs (Navier-Stokes, Eqs. (28) and (29)) and another for the species transport PDE (Eq. (30)). Because of the one-way coupling (fluid flow influences mass transport but not vice versa for a dilute system) and since no flow-field parameter inference is required, we first train the fluid flow PINN using the fixed parameters and boundary conditions described earlier. Its output is then used to compute the residual of Eq. (30), which in turn guides the training of two distinct mass transport PINNs: one for computing sensitivity derivatives and another for parameter estimation.

Fluid Flow PINN

The fluid flow PINN admits two inputs, x and y, and produces: $\hat{\mathbf{v}}$, and $\hat{p}$. The ˆ symbol is used to denote the PINN approximation. The architecture is a fully connected neural network with 8 hidden layers of 60 neurons each, using hyperbolic tangent activation functions. The loss function minimized during training is:

$$\begin{aligned}
\mathcal{L}(\theta) = &\, w_{in} \mathcal{L}_{in}(\theta) + w_{out} \mathcal{L}_{out}(\theta) + w_{wall,up} \mathcal{L}_{wall,up}(\theta) + w_{wall,low} \mathcal{L}_{wall,low}(\theta) \\
&+ w_{wall,obst.} \mathcal{L}_{wall,obst.}(\theta) + w_{ns} \mathcal{L}_{ns}(\theta) + w_{cont.} \mathcal{L}_{cont.}(\theta),
\end{aligned} \tag{31}$$

where $\mathcal{L}_{ns}(\theta)$ and $\mathcal{L}_{cont.}(\theta)$ correspond to the residuals of Eqs. (28) and (29), and $\mathcal{L}_{in}(\theta)$, $\mathcal{L}_{out}(\theta)$, $\mathcal{L}_{wall,up}(\theta)$, $\mathcal{L}_{wall,low}$, and $\mathcal{L}_{wall,obst.}$ correspond to the inlet, outlet and wall boundary condition residuals, respectively. Analytical expressions for each loss term are provided in Section II.1 of the Supplementary Material. The PINN model is trained for 35,000 iterations with the Adam optimizer, followed by 2,000 iterations with L-BFGS for improved accuracy. We also employ RAR-D (adaptive collocation point sampling) and an adaptive weight strategy (see Section 2.3). Complete hyperparameter settings are listed in Table 3. Training requires approximately 95 minutes. The magnitude of the predicted flow field, $|\hat{\mathbf{v}}| = \sqrt{\hat{v}_x^2 + \hat{v}_y^2}$, is visualized and compared with the corresponding numerical solution in Fig. 6 showing the high accuracy of the fluid flow PINN model.

Mass-Transport Sensitivity PINN

We next construct a PINN model to compute the sensitivity of species concentration with respect to the dimensionless parameters Pe and Da. This model admits five inputs: x, y, t, Pe, and Da, and outputs $\hat{c}$. Its architecture consists of 5 hidden layers with 100 neurons each and tanh activations. The loss function is:

Table 3
Hyperparameters for different PINN architectures and training settings in the 2D reaction-diffusion-advection problem.

PINN hyperparameter	Fluid Flow PINN	Mass Transport Sensitivity PINN	Mass Transport Inference PINN
Hidden layers	8	5	5
Neurons per layer	60	100	100
Inputs	2 (x, y)	5 (x, y, t, Pe, Da)	3 (x, y, t)
Outputs	$\hat{v}, \hat{p}$	$\hat{c}$	$\hat{c}$
Activation function	tanh	tanh	tan
Optimizer	Adam and L-BFGS	Adam and L-BFGS	L-BFGS
Optimizer iterations	35000 (Adam) and 2000 (L-BFGS)	35000 (Adam) and 1000 (L-BFGS)	2000
Number of initially sampled training points	$N_f = 40000$ (collocation) $N_{in} = 1500$ (inlet) $N_{out} = 1500$ (outlet) $N_{wall} = 500$ (channel wall) $N_{obst} = 100$ (obstacle wall)	$N_f = 55000$ (collocation) $N_{in} = 7000$ (inlet) $N_{out} = 3000$ (outlet) $N_{wall} = 4000$ (channel wall) $N_{obst} = 3000$ (obstacle wall) $N_{init} = 15000$ (initial condition)	$N_f = 75000$ (collocation) $N_{in} = 8000$ (inlet) $N_{out} = 8000$ (outlet) $N_{wall} = 8000$ (channel wall) $N_{obst} = 3000$ (obstacle wall) $N_{init} = 15000$ (initial condition)
Dynamic Weight Strategy	Yes	Yes	No
RAR-D	Yes	Yes	Yes
Frequency of sampling new training points	Every 2000 (Adam) training iterations	Every 2000 (Adam) training iterations	Every 100 (L-BFGS) training iterations
Number of added training points with RAR-D	300 collocation points 20 inlet points 30 wall points	1000 collocation points 300 inlet points 300 wall points 800 initial condition points	750 collocation points 50 inlet points 50 wall points 150 initial points

$$\mathcal{L}(\theta) = w_f \, \mathcal{L}_f(\theta) + w_{init} \, \mathcal{L}_{init}(\theta) + w_{in} \, \mathcal{L}_{in}(\theta) + w_{out} \, \mathcal{L}_{out}(\theta) + w_{wall,up} \, \mathcal{L}_{wall,up}(\theta)$$
$$+ w_{wall,low} \, \mathcal{L}_{wall,low}(\theta) + w_{obst} \, \mathcal{L}_{obst}(\theta) + w_{sens,Pe} \, \mathcal{L}_{sens,Pe} + w_{sens,Da} \, \mathcal{L}_{sens,Da}, \tag{32}$$

where $\mathcal{L}_f(\theta)$ is the residual of Eq. (30), $\mathcal{L}_{init}(\theta)$ enforces the initial condition, $\mathcal{L}_{in}(\theta), \mathcal{L}_{out}(\theta), \mathcal{L}_{wall,up}(\theta), \mathcal{L}_{wall,low}(\theta)$, $\mathcal{L}_{obst}(\theta)$ correspond to boundary condition residuals for the species concentration at the inlet, outlet and walls of the channel. The sensitivity terms $\mathcal{L}_{sens,Pe}, \mathcal{L}_{sens,Da}$ are sums of the derivatives of all residuals with respect to Pe and Da, respectively. Details are given in Section II.2 of the Supplementary Material; full training parameters are listed in Table 3. Since Pe and Da are initially unknown, this PINN model is trained using initial estimates (here, we use $Pe = 7.0$ and $Da = 18.0$). As discussed in Section 2.3, we assume that the maxima locations of the Gram determinant remain nearly unchanged when computed with these estimates instead of true values. Training requires approximately 270 minutes.

Once trained, the model provides sensitivity functions $s_{Pe}(x, y, t) = \frac{\partial \hat{c}}{\partial Pe}(x, y, t)$ and $s_{Da}(x, y, t) = \frac{\partial \hat{c}}{\partial Da}(x, y, t)$ computed via automatic differentiation. These functions are used to assemble the FIM (Eqs. (5) and (6)), and evaluate its determinant for sensor placement. For a single sensor, the Gram determinant depends only on (x_1, y_1), and its spatial distribution is illustrated in Fig. 7.

When multiple sensors are considered, the optimization of the Gram determinant becomes multidimensional. To address this, we employ the Covariance Matrix Adaptation Evolution Strategy (CMA-ES) (Hansen, 2016), a derivative-free algorithm well suited for high-dimensional, non-convex, and nonlinear problems (Python package *pycma* (Hansen et al., 2019)). We first examine the case of three optimal sensor locations and compare the inference results against a configuration of three intuitively placed sensors around the obstacle (see Fig. 8). Pseudo-experimental data are generated by computational experiments using the finite element based commercial software COMSOL $^{®}$ setting $Pe = 12.0$ and $Da = 22.0$ (target values to be inferred by our PINN-based framework). Virtual sensors record species concentration every 3 seconds.

Table 4
Inferred Pe and Da values and relative error from ground truth using data (noise-free) for different sensor counts.

Number of sensors	Pe (12.0)		Da (22.0)	
	Optimal sensors	Intuitive sensors	Optimal sensors	Intuitive sensors
1	11.36 (5.33%)	11.09 (7.58%)	20.79 (5.50%)	20.33 (7.59%)
2	11.62 (3.17%)	10.65 (11.25%)	21.08 (4.18%)	19.28 (12.36%)
3	11.80 (1.67%)	11.09 (7.58%)	21.49 (2.32%)	20.23 (8.05%)
5	11.98 (0.17%)	11.34 (5.50%)	21.78 (1.00%)	20.72 (5.82%)

Mass-Transport PINN for Parameter Estimation

Here, we train a PINN to infer the unknown parameters. This neural network has the same architecture as the sensitivity PINN, but with only spatio-temporal inputs (x, y, t). Its loss function excludes the sensitivity terms ($\mathcal{L}_{\text{sens},Pe}$ and $\mathcal{L}_{\text{sens},Da}$) and instead incorporates a data loss term:

$$\mathcal{L}_{data}(\theta) = \frac{1}{N_{data}} \sum_{i=1}^{N_{data}} \left| \hat{c}(x_{data}^i, y_{data}^i, t_{data}^i) - c_{data}^i \right|^2 . \tag{33}$$

For computational efficiency, we first pre-train this network on the forward problem with initial parameter estimates, then reuse this state for parameter estimation. During fine-tuning, the weights and biases of the first three layers are frozen (see Section 2.3). The dynamic weight strategy is disabled, and to emphasize observational data we set $w_{data} = 100$ (weight of data loss term), while keeping all other weights equal to 1. Further training details are provided in Table 3.

The inference results for the three-sensor configurations are shown in Fig. 9. Both parameters are estimated with higher accuracy when using optimally placed sensors. In addition, the three optimally placed sensors provide sufficient information for the PINN to reconstruct the concentration field, as illustrated in Fig. 10.

To study the effect of the number of sensors, we repeat the procedure for 1, 2 and 5 sensors, each time optimizing sensor placement using CMA-ES and comparing the results with intuitive arrangements. For completeness, we show the locations of optimally placed sensors and the intuitively selected arrangements for 1,2,3 and 5 sensors in Fig. 11.

Table 4 summarizes the inferred parameter values, showing that optimally placed sensors consistently yield more accurate estimates. Notably, adding more *intuitively* placed sensors does not necessarily improve performance, while accuracy increases monotonically with the number of *optimally* chosen sensors.

We further tested robustness to noise adding Gaussian noise to the COMSOL-generated pseudo-experimental concentration data. Each measurement was drawn from:

$$\tilde{c}_{data}^i \sim \mathcal{N}(c_{data}^i, (0.1c_{data}^i)^2). \tag{34}$$

To account for the noisy data, we repeated the parameter estimation training five times for each configuration. Fig. 12 depicts results for the three-sensor case, showing mean trajectories and standard deviations. Optimal sensors again led to more accurate averages, particularly for Da, which corresponds to the nonlinear term of Eq. (30). The same trends hold for the 1-, 2-, and 5-sensor cases (Table 5). Fig. 13 compares the PINN solution (fitted to noisy data from 3 optimal sensors) with the FEM solution at the true parameters. One can observe that the PINN predictions are in close agreement with the sensor data in terms of overall trends. Each estimation experiment required approximately 100 minutes of training.

4. Conclusions

In this work, we develop a novel ML-based methodology for optimal sensor placement in large-scale distributed parameter systems for efficient parameter estimation. We integrate the D-optimal criterion for sensor placement into the PINN framework, with the goal of leveraging PINNs' parameter estimation capabilities using minimal observational

Table 5

Mean Inferred Pe and Da values (with standard deviation) using noisy data for different sensor counts.

Number of sensors	Pe (12.0)		Da (22.0)	
	Optimal sensors	Intuitive sensors	Optimal sensors	Intuitive sensors
1	10.73 ± 0.61	10.73 ± 0.19	20.30 ± 1.14	19.47 ± 1.02
2	11.38 ± 0.35	11.38 ± 0.76	20.20 ± 0.97	20.01 ± 1.07
3	12.01 ± 0.26	11.18 ± 0.60	21.97 ± 0.75	19.59 ± 1.94
5	11.96 ± 0.43	11.12 ± 0.38	21.26 ± 0.55	20.11 ± 0.97

data. Our approach first determines optimal sensor locations based on an *a priori* estimate for the parameters of interest, and then identifies these parameters using data collected from those locations.

To solve the optimal sensor placement problem, we train a PINN that takes as input both the parameters of interest and the spatio-temporal coordinates. This design enables the computation of sensitivity functions via automatic differentiation, which are then used to select the optimal sensor positions. For parameter inference, we employ a standard PINN architecture trained on data sampled from either optimally placed or intuitively chosen virtual sensors generated from numerical solutions.

We evaluate the framework on two illustrative case studies: A 1D steady-state and a 2D transient reaction-diffusion-advection problem. In the 1D case, we estimate the Péclet number using a single sensor. Placement at the optimal location yields a relative error of only 0.20%, whereas placement at the outlet produces a substantially larger error of 84.7%, underscoring the importance of optimal sensor positioning. In the 2D transient case, we jointly estimate the Péclet and Damköhler numbers using sensor configurations of 1, 2, 3, and 5 sensors. With noiseless data, optimal sensor placements consistently provide more accurate estimates, and accuracy improves as the number of sensors increases. Introducing measurement noise preserved these trends.

Training a PINN to compute sensitivity functions is computationally intensive at the outset (≈ 270 minutes), owing to the additional loss terms requiring derivatives of all residuals with respect to all parameters of interest. However, once trained, transfer learning enables rapid re-training, offering substantial flexibility. This allows the framework to adapt efficiently to changes in boundary or initial conditions, modifications to system geometry, or variations in the underlying physics (e.g., altered reaction kinetics), without restarting training from scratch. Moreover, since PINNs are mesh-less, sensitivity functions can be computed at any spatio-temporal location.

Overall, our findings demonstrate that PINNs can be effectively used to compute sensitivity functions for optimal sensor placement in parameter estimation. Data collected at these locations significantly improve estimation accuracy, even under measurement noise. Beyond the benchmark problems considered here, the framework can be extended to more complex systems with multiple unknown parameters or partially defined models (e.g., unknown kinetics in plasma reactors), where data acquisition is costly or limited.

Acknowledgements
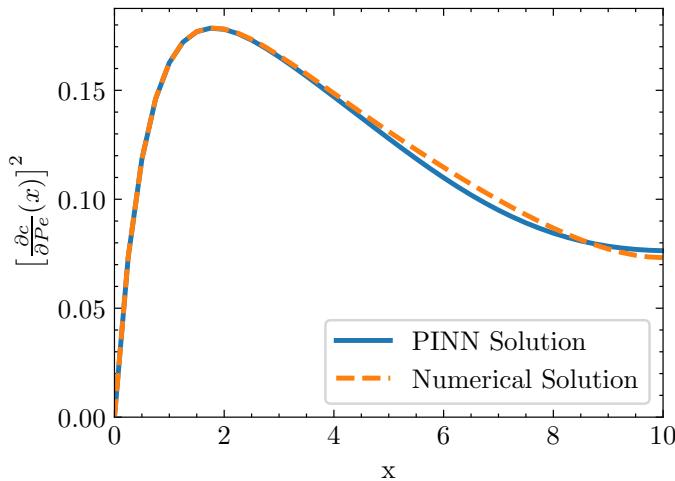
Figure 2: Spatial profile of the FIM trace computed by PINNs and numerically for $Pe = 0.1$ (*a priori* estimate) and $Da = 1.0$.
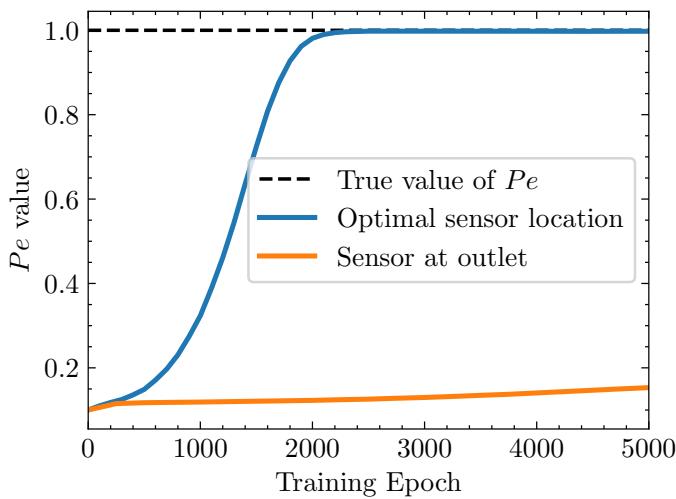

Figure 3: Inference of Pe vs. PINN training epochs with sensor placed at the FIM trace maximum ($x^* = 1.81$ -blue curve) versus at the outlet ($x^* = 10.0$ -red curve)
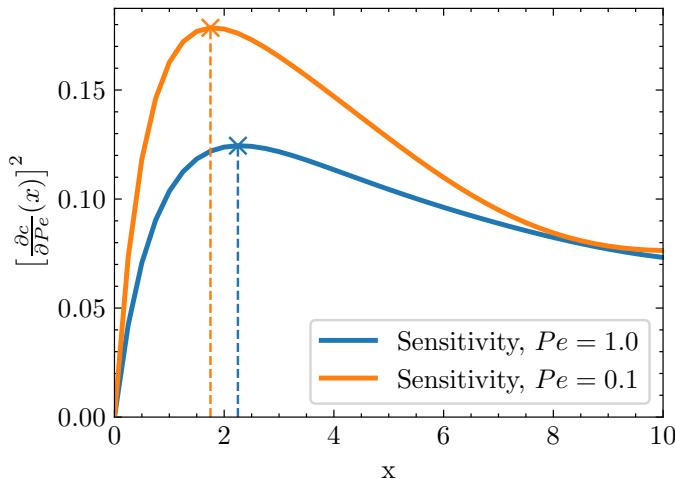
Figure 4: FIM trace for the *a priori* estimate $Pe = 0.1$ and true value $Pe = 1.0$.
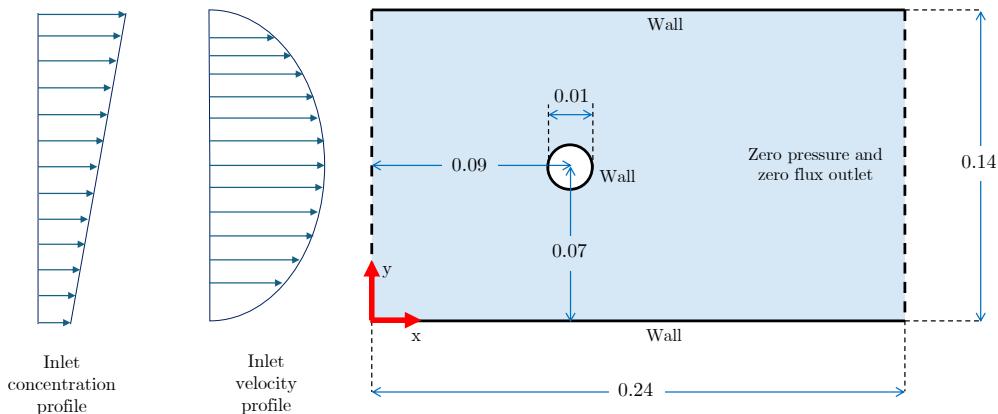

Figure 5: Computational domain: the fluid enters the channel with a parabolic velocity profile at the horizontal direction carrying a reactive species, flows past a fixed obstacle, and undergoes transport and reaction.
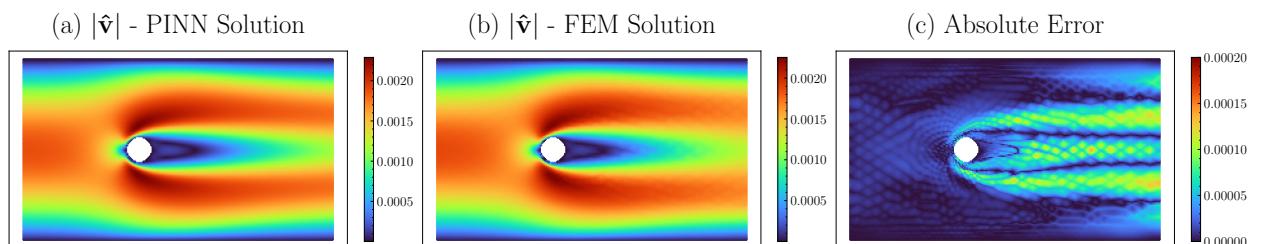
Figure 6: Magnitude of the velocity field $|\hat{\mathbf{v}}|$: (a) PINN prediction of the fluid flow, (b) FEM numerical solution and (c) absolute error of PINN prediction relative to the FEM solution.
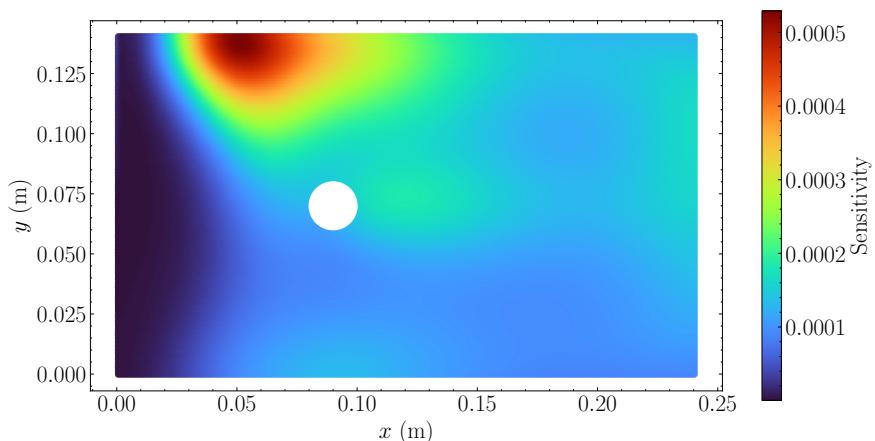
Figure 7: Spatial profile of Gram determinant computed with sensitivity PINN for a priori estimate of Pe (7.0) and Da (18.0)
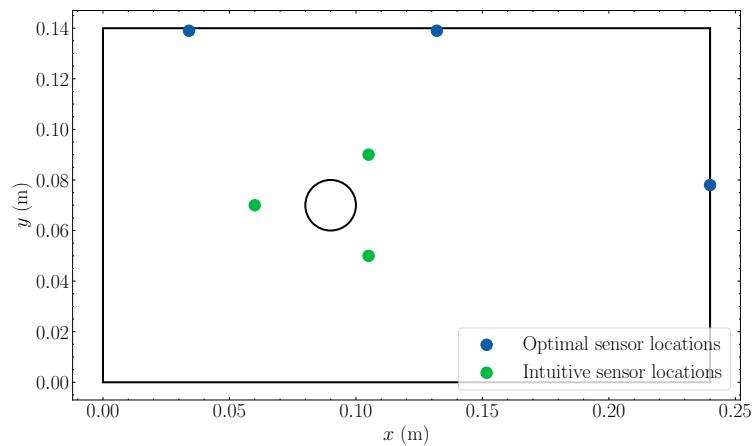
Figure 8: Optimally selected and intuitively placed sensor locations for the 2D set-up
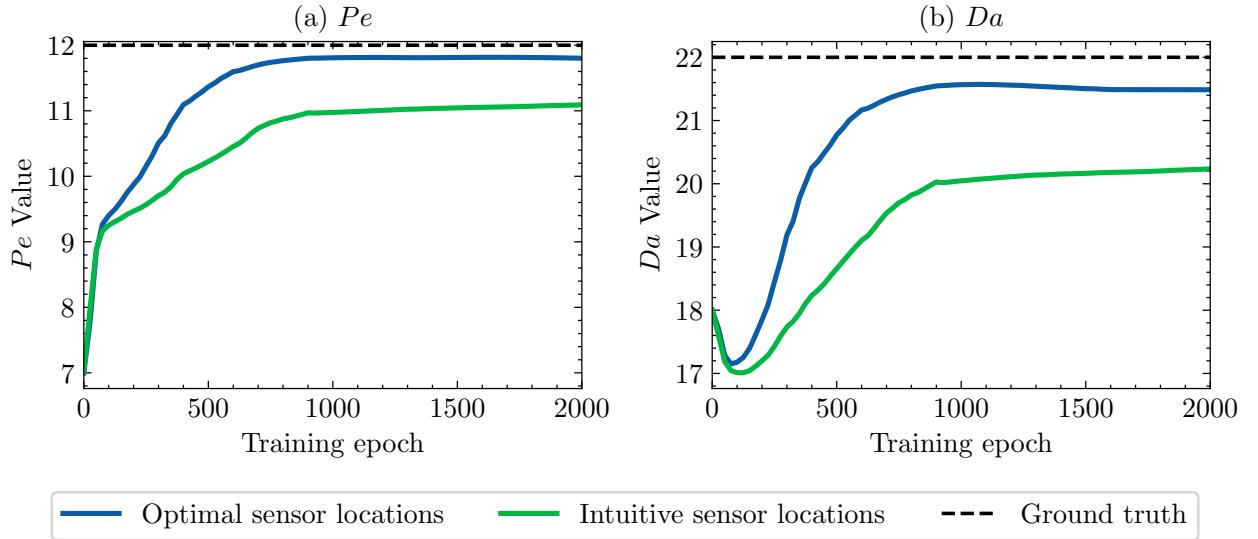
Figure 9: Parameter inference using data from optimally placed sensors versus intuitive placements: (a) Pe, (b) Da.
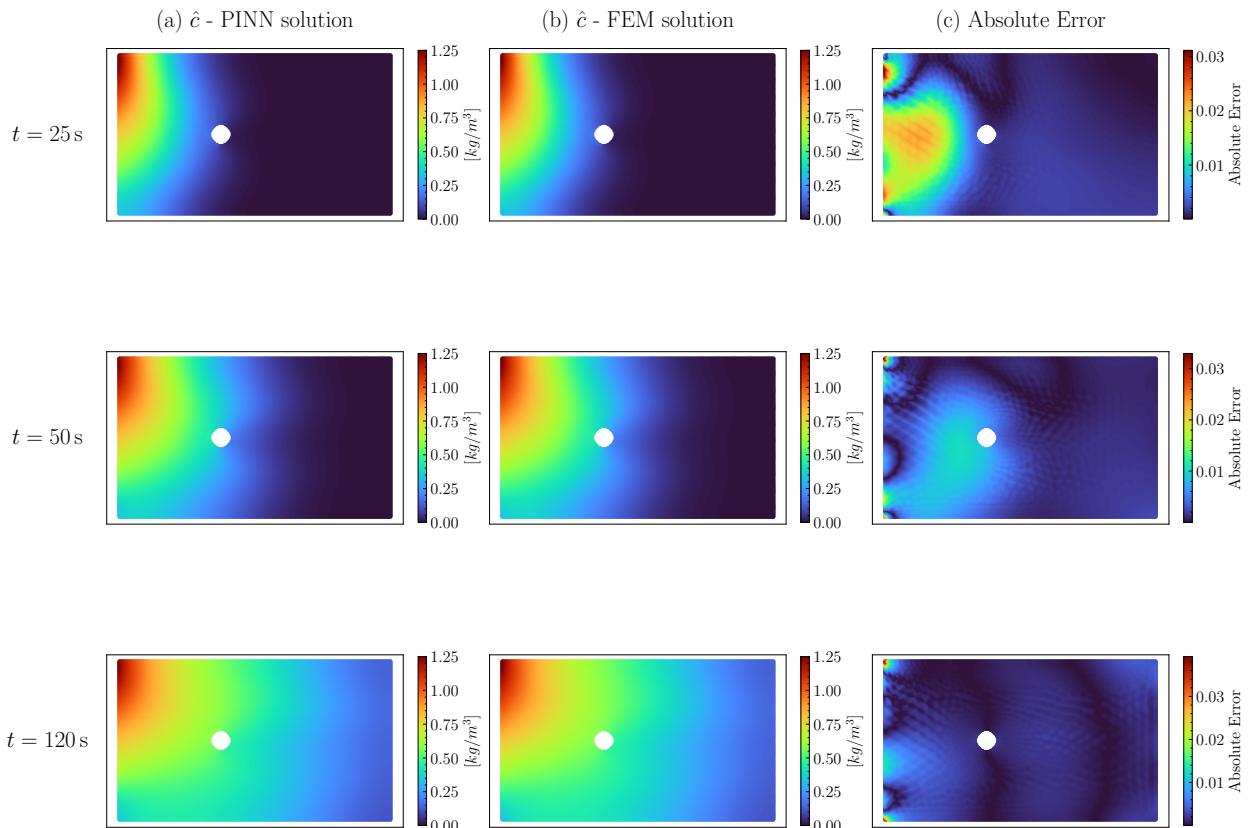

Figure 10: Predicted Concentration field $\hat{c}(x, y, t)$ at $t = 25, 50, 120$ s: (a) PINN prediction trained with data from optimal sensors, (b) FEM numerical solution for true parameter values, and (c) Absolute error ($|\hat{c}_{PINN} - \hat{c}_{FEM}|$).
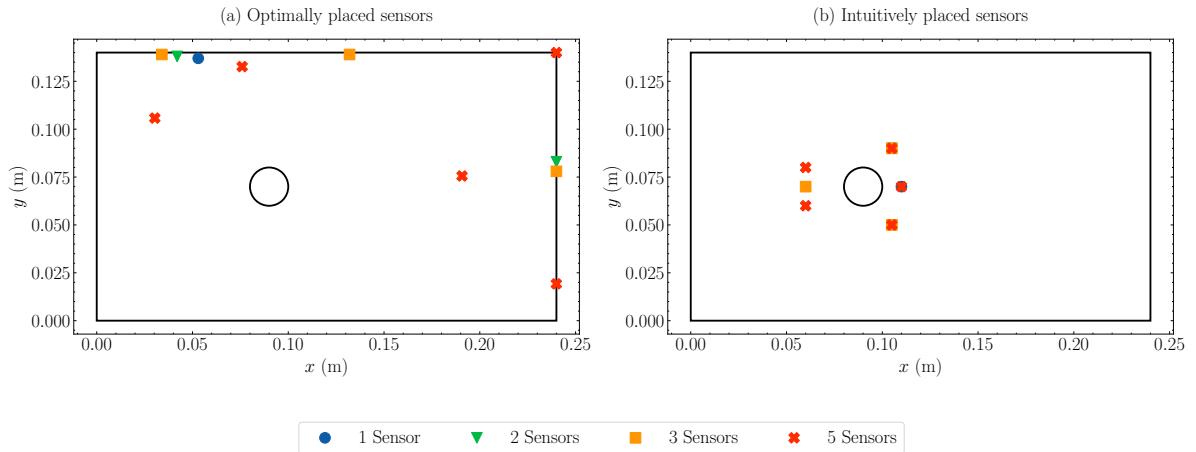
Figure 11: (a) Optimally selected and (b) intuitively placed sensor locations for the 2D set-up using 1 sensor (blue circle), 2 sensors (green triangles), 3 sensors (orange rectangles) and 5 sensors (red crosses).
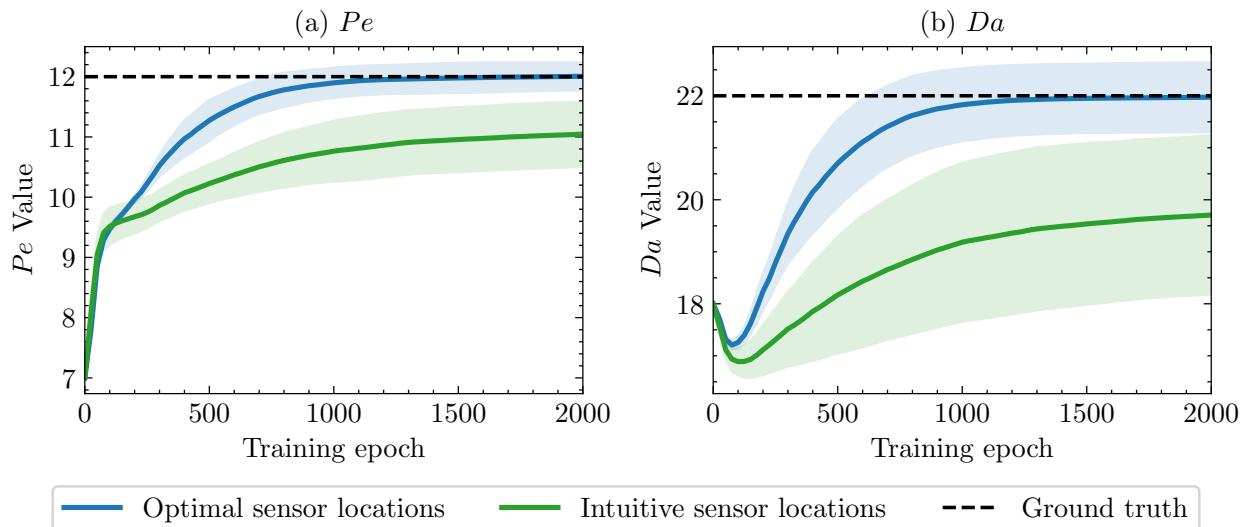

Figure 12: Mean and standard deviation (shaded area) of parameter inference with noisy data from optimal sensor locations versus intuitive sensor placements: (a) Pe, (b) Da
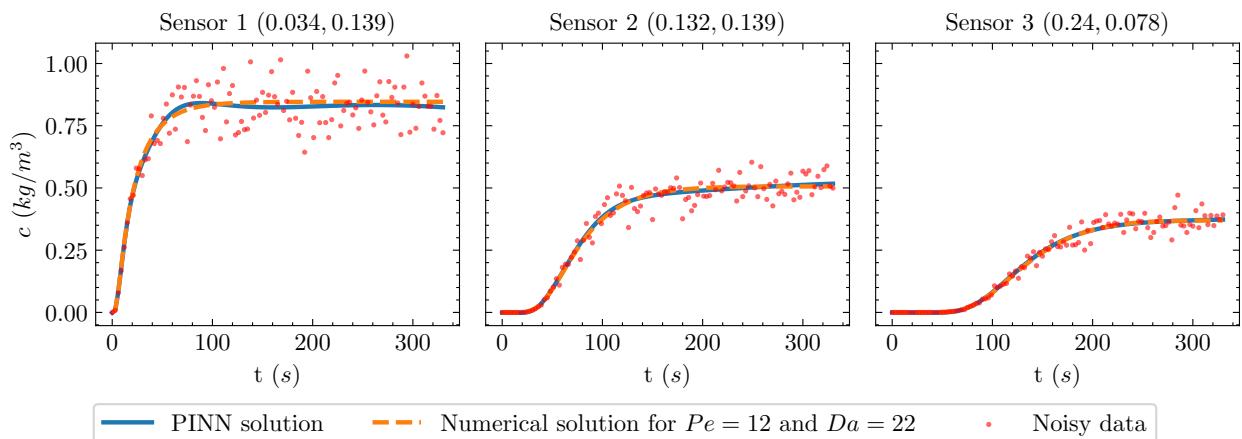
Figure 13: PINN prediction fitted to noisy data from 3 optimally placed sensors, compared with FEM solution at true parameters.

References

Alaña, J.E., Theodoropoulos, C., 2011. Optimal location of measurements for parameter estimation of distributed parameter systems. Computers & Chemical Engineering 35, 106–120. URL: https://www.sciencedirect.com/science/article/pii/S0098135410001547, doi:https://doi.org/10.1016/j.compchemeng.2010.04.014.

Alaña, J.E., Theodoropoulos, C., 2012. Optimal spatial sampling scheme for parameter estimation of nonlinear distributed parameter systems. Computers & Chemical Engineering 45, 38–49. doi:https://doi.org/10.1016/j.compchemeng.2012.04.014.

Alonso, A.A., Kevrekidis, I.G., Banga, J.R., Frouzakis, C.E., 2004. Optimal sensor location and reduced order observer design for distributed process systems. Computers & chemical engineering 28, 27–35.

Bard, Y., 1974. Nonlinear parameter estimation. volume 1209. Academic press New York.

Berardi, M., Difonzo, F.V., Icardi, M., 2025. Inverse physics-informed neural networks for transport models in porous materials. Computer Methods in Applied Mechanics and Engineering 435, 117628.

Biegler, L., Damiano, J., Blau, G., 1986. Nonlinear parameter estimation: a case study comparison. AIChE Journal 32, 29–45.

Blei, D.M., Kucukelbir, A., McAuliffe, J.D., 2017. Variational inference: A review for statisticians. Journal of the American statistical Association 112, 859–877.

Bottou, L., 2010. Large-scale machine learning with stochastic gradient descent, in: Proceedings of COMPSTAT'2010: 19th International Conference on Computational StatisticsParis France, August 22-27, 2010 Keynote, Invited and Contributed Papers, Springer. pp. 177–186.

Cai, S., Wang, Z., Wang, S., Perdikaris, P., Karniadakis, G.E., 2021. Physics-informed neural networks for heat transfer problems. Journal of Heat Transfer 143, 060801.

Chang, S., Agarwal, P., McCready, C., Ricardez-Sandoval, L., Budman, H., 2025. Robust pinn modeling via sensitivity-based adaptive sampling: Integration of optimal sensor placement and structural uncertainty handling. Journal of Process Control 152, 103493. URL: https://www.sciencedirect.com/science/article/pii/S0959152425001210, doi:https://doi.org/10.1016/j.jprocont.2025.103493.

Chaturantabut, S., Sorensen, D.C., 2010. Nonlinear model reduction via discrete empirical interpolation. SIAM Journal on Scientific Computing 32, 2737–2764.

Coleman, M.C., Block, D.E., 2006. Bayesian parameter estimation with informative priors for nonlinear systems. AIChE journal 52, 651–667.

Courant, R., Hilbert, D., 1989. The Algebra of Linear Transformations and Quadratic Forms. John Wiley & Sons, Ltd. chapter 1. pp. 1–47. doi:https://doi.org/10.1002/9783527617210.ch1.

Englezos, P., Kalogerakis, N., 2000. Applied parameter estimation for chemical engineers. CRC Press.

Forootani, A., Kapadia, H., Chellappa, S., Goyal, P., Benner, P., 2024. Gs-pinn: Greedy sampling for parameter estimation in partial differential equations. arXiv preprint arXiv:2405.08537 .

Franceschini, G., Macchietto, S., 2008. Model-based design of experiments for parameter precision: State of the art. Chemical Engineering Science 63, 4846–4872. URL: https://www.sciencedirect.com/science/article/pii/S0009250907008871, doi:https://doi.org/10.1016/j.ces.2007.11.034. model-Based Experimental Analysis.

Goswami, S., Anitescu, C., Chakraborty, S., Rabczuk, T., 2020. Transfer learning enhanced physics informed neural network for phase-field modeling of fracture. Theoretical and Applied Fracture Mechanics 106, 102447. URL: https://www.sciencedirect.com/science/article/pii/S016784421930357X, doi:https://doi.org/10.1016/j.tafmec.2019.102447.

Hanna, J.M., Aguado, J.V., Comas-Cardona, S., Askri, R., Borzacchiello, D., 2024. Sensitivity analysis using physics-informed neural networks. Engineering Applications of Artificial Intelligence 135, 108764.

Hansen, N., 2016. The cma evolution strategy: A tutorial. arXiv preprint arXiv:1604.00772 .

Hansen, N., Akimoto, Y., Baudis, P., 2019. CMA-ES/pycma on Github. Zenodo, DOI:10.5281/zenodo.2559634. URL: https://doi.org/10.5281/zenodo.2559634, doi:10.5281/zenodo.2559634.

Hastings, W.K., 1970. Monte carlo sampling methods using markov chains and their applications. Biometrika 57, 97–109. URL: https://doi.org/10.1093/biomet/57.1.97, doi:10.1093/biomet/57.1.97, arXiv:https://academic.oup.com/biomet/article-pdf/57/1/97/23940249/57-1-97.pdf.

Heredia-Zavoni, E., Esteva, L., 1998. Optimal instrumentation of uncertain structural systems subject to earthquake ground motions. Earthquake engineering & structural dynamics 27, 343–362.

Hermanto, M.W., Kee, N.C., Tan, R.B., Chiu, M.S., Braatz, R.D., 2008. Robust bayesian estimation of kinetics for the polymorphic transformation of l-glutamic acid crystals. AIChE Journal 54, 3248–3259.

Hornik, K., Stinchcombe, M., White, H., 1989. Multilayer feedforward networks are universal approximators. Neural networks 2, 359–366.

Hu, Z., Shukla, K., Karniadakis, G.E., Kawaguchi, K., 2024. Tackling the curse of dimensionality with physics-informed neural networks. Neural Networks 176, 106369.

Huang, H., Li, Y., Song, R., Ren, J., Yu, H., Zhou, X., He, C., 2025. Inverse design of the membrane reactors enabled by an inverse-forward physics-informed learning framework. Chemical Engineering Science 316, 121910.

Kalyanaraman, J., Fan, Y., Labreche, Y., Lively, R.P., Kawajiri, Y., Realff, M.J., 2015. Bayesian estimation of parametric uncertainties, quantification and reduction using optimal design of experiments for co2 adsorption on amine sorbents. Computers & chemical engineering 81, 376–388.

Kravaris, C., Hahn, J., Chu, Y., 2013. Advances and selected recent developments in state and parameter estimation. Computers & Chemical Engineering 51, 111–123. URL: https://www.sciencedirect.com/science/article/pii/S0098135412001779, doi:https://doi.org/10.1016/j.compchemeng.2012.06.001. cPC VIII.

Laubscher, R., 2021. Simulation of multi-species flow and heat transfer using physics-informed neural networks. Physics of Fluids 33.

Lenk, P., Orme, B., 2009. The value of informative priors in bayesian inference with sparse data. Journal of Marketing Research 46, 832–845.

Li, S., Feng, X., 2022. Dynamic weight strategy of physics-informed neural networks for the 2d navier–stokes equations. Entropy 24. doi:10.3390/e24091254.

Liao, S., Xue, T., Jeong, J., Webster, S., Ehmann, K., Cao, J., 2023. Hybrid thermal modeling of additive manufacturing processes using physics-informed neural networks for temperature prediction and parameter identification. Computational Mechanics 72, 499–512.

Mao, Z., Jagtap, A.D., Karniadakis, G.E., 2020. Physics-informed neural networks for high-speed flows. Computer Methods in Applied Mechanics and Engineering 360, 112789. URL: https://www.sciencedirect.com/science/article/pii/S0045782519306814, doi:https://doi.org/10.1016/j.cma.2019.112789.

Mehra, R., 1974. Optimal inputs for linear system identification. IEEE Transactions on Automatic Control 19, 192–200.

Myung, I.J., 2003. Tutorial on maximum likelihood estimation. Journal of mathematical Psychology 47, 90–100.

Nahor, H., Scheerlinck, N., Van Impe, J.F., Nicolaï, B., 2003. Optimization of the temperature sensor position in a hot wire probe set up for estimation of the thermal properties of foods using optimal experimental design. Journal of food engineering 57, 103–110.

Ngo, S.I., Lim, Y.I., 2021. Solution and parameter identification of a fixed-bed reactor model for catalytic co2 methanation using physics-informed neural networks. Catalysts 11, 1304.

Papadimitriou, C., Beck, J.L., Au, S.K., 2000. Entropy-based optimal sensor location for structural model updating. Journal of Vibration and Control 6, 781–800.

Papamakarios, G., Nalisnick, E., Rezende, D.J., Mohamed, S., Lakshminarayanan, B., 2021. Normalizing flows for probabilistic modeling and inference. Journal of Machine Learning Research 22, 1–64.

Paszke, A., Gross, S., Massa, F., Lerer, A., Bradbury, J., Chanan, G., Killeen, T., Lin, Z., Gimelshein, N., Antiga, L., et al., 2019. Pytorch: An imperative style, high-performance deep learning library. Advances in neural information processing systems 32.

Qureshi, Z., Ng, T., Goodwin, G., 1980. Optimum experimental design for identification of distributed parameter systems. International Journal of Control 31, 21–29.

Raissi, M., Perdikaris, P., Karniadakis, G., 2019. Physics-informed neural networks: A deep learning framework for solving forward and inverse problems involving nonlinear partial differential equations. Journal of Computational Physics 378, 686–707. URL: https://www.sciencedirect.com/science/article/pii/S0021999118307125, doi:https://doi.org/10.1016/j.jcp.2018.10.045.

Raissi, M., Yazdani, A., Karniadakis, G.E., 2020. Hidden fluid mechanics: Learning velocity and pressure fields from flow visualizations. Science 367, 1026–1030. URL: https://www.science.org/doi/abs/10.1126/science.aaw4741, doi:10.1126/science.aaw4741, arXiv:https://www.science.org/doi/pdf/10.1126/science.aaw4741.

Vande Wouwer, A., Point, N., Porteman, S., Remy, M., 2000. An approach to the selection of optimal sensor locations in distributed parameter systems. Journal of Process Control 10, 291–300.

Walter, É., Pronzato, L., 1990. Qualitative and quantitative experiment design for phenomenological models—a survey. Automatica 26, 195–213.

Wang, S., Sankaran, S., Wang, H., Perdikaris, P., 2023. An expert's guide to training physics-informed neural networks.

Wu, C., Zhu, M., Tan, Q., Kartha, Y., Lu, L., 2023. A comprehensive study of non-adaptive and residual-based adaptive sampling for physics-informed neural networks. Computer Methods in Applied Mechanics and Engineering 403, 115671.

Yin, M., Zheng, X., Humphrey, J.D., Karniadakis, G.E., 2021. Non-invasive inference of thrombus material properties with physics-informed neural networks. Computer Methods in Applied Mechanics and Engineering 375, 113603. URL: https://www.sciencedirect.com/science/article/pii/S004578252030788X, doi:https://doi.org/10.1016/j.cma.2020.113603.

Zhuang, F., Qi, Z., Duan, K., Xi, D., Zhu, Y., Zhu, H., Xiong, H., He, Q., 2021. A comprehensive survey on transfer learning. Proceedings of the IEEE 109, 43–76. doi:10.1109/JPROC.2020.3004555.